Development and characteristics of a membraneless microfluidic fuel cell array

Huizhi Wang [a,c], Shunjie Gu [b,c], Dennis Y. C. Leung [c], Hong Xu [b], Michael K. H. Leung [d], Li Zhang [b], Jin Xuan [a,b,*]

[a] School of Engineering and Physical Sciences, Heriot-Watt University, Edinburgh, EH14 4AS, UK

[b] State-Key Laboratory of Chemical Engineering, School of Mechanical and Power Engineering, East China University of Science and Technology, Shanghai 200237, China

[c] Department of Mechanical Engineering, The University of Hong Kong, Pokfulam Road, Hong Kong

[d] Ability R&D Energy Research Center, School of Energy and Environment, City University of Hong Kong, Kowloon Tong, Hong Kong

[*] Corresponding author. State-Key Laboratory of Chemical Engineering, School of Mechanical and Power Engineering, East China University of Science and Technology, Shanghai 200237, China. Tel.: +86 21 64252847; Fax: +86 21 64253810.

Email addresses: jxuan@ecust.edu.cn

Abstract

Membraneless microfluidic fuel cells (M^2FCs) are promising portable power sources, but they suffer from limited scalability. This paper presents a scaling-out strategy for general M^2FC applications with their characteristics studied by both experiments and mathematical modeling. The present strategy addresses the issues of flow distribution non-uniformity and shunt current losses by integrating a well-designed fluid circuit. With the present strategy, parallel and series connections of four cells in an array results in a scaling-out efficiency of 93% and 82%, respectively. The effects of different parameters on the array performance as well as further device scalability are also investigated in this paper. Preferable conditions for

the array operation include a high branch ionic resistance, small unit cell difference and high unit-cell performance, which can be achieved by appropriately designing the branch geometry, employing high-precision fabrication / assembly techniques and improving the single-cell materials / chemistries. It is expected that the present array can be incremented to 50 cells or above in series with over 75% efficiency as long as there is sufficiently high branch resistance or cell performance.

Key words: Membraneless fuel cell; Formic acid; Hydrogen peroxide; Microfluidics; Scale out; Shunt current analysis

1. Introduction

Membraneless microfluidic fuel cells (M^2FCs) have received much attention in recent years as an alternative power source for portable electronic applications. Unlike conventional fuel cells, M^2FCs work without a polymer electrolyte membrane (PEM) and utilize the interface between microflow streams instead as their reactant separator and ion conductor. A typical M^2FC operation involves anolyte (containing fuel) and catholyte (containing oxidant) streams flowing side-by-side in a microfluidic channel against their respective electrodes (*i.e.*, anode and cathode). The laminar nature of microflows restricts the mixing of the streams to an interfacial width located between the two electrodes and thus prevents reactant crossover, which hinders cell performance. In addition, the required ionic conduction from one electrode to the other is maintained by an electrolyte contained in the streams. Therefore, M^2FCs offer a number of advantages over conventional PEM fuel cells, including (i) the elimination of membrane-related technical issues such as water management, membrane contamination and fuel crossover; (ii) simple structure; (iii) low cost; and (iv) high fuel/media flexibility [1-3]. In the past decade since their first appearance [4], M^2FCs have undergone substantial

development in their configurations [5-10], fabrication [11-12], chemistries [13-15] and electrode catalysts [16-20], resulting in a hundred-fold increase in area-specific power and nearly complete single-pass fuel conversion. A comprehensive summary of past M^2FC research is given by two recent review papers [21, 22], where more detailed information on the governing physics, development milestones as well as perspectives of M^2FC technologies can be found. Despite these remarkable advancements, the practical application of M^2FCs is still severely limited because of their small overall power output associated with the inherent cell size. Dimensional scale-up of M^2FCs to achieve satisfactory output has been proven infeasible as micro-scale geometries are prerequisite to ensuring the basic device functionality. In addition, the scale-up process is inevitably accompanied by significant power and energy losses attributed to the boundary layer growth and diffusive interface broadening inside the cell [2, 7, 23].

To overcome the limitations in the scale-up of M^2FCs, a so-called “scale-out” approach has been employed to increase the M^2FC output. This approach involves creating an array or a stack of multiple cells connected in series, parallel or mixture of both series and parallel. Up to now, several M^2FC scaling-out strategies have been proposed, but they are either limited to specific designs of M^2FC or suffer shortcomings in practical operation and further expansion. Salloum and Posner [24] reported a two-cell planar array of M^2FC based on their previously developed multi-pass single cell design [10]. In the array design, unit cells were fluidically connected in series to enhance the overall fuel utilization by reusing the unreacted fuels from the first cell for the other cell. Although nearly doubled fuel utilization and peak power relative to a single cell were achieved in the array with a parallel electrical connection, this only occurred at a certain combination of reactant and electrolyte speeds. In most instances, the downstream cell exhibited much lower performance than the first cell because of lower reactant concentrations due to dilution and utilization from the first cell, which can

significantly degrade overall power efficiency (even worse in the series electrical connection) and prohibit further increases in cell number. Moreover, the requirement of a third electrolyte stream in their design considerably complicates the device operation. The multi-outlet structure of the array also tremendously increases the difficulties in pressure and flow managements. Alternatively, Moore et al. demonstrated a vertical stack of planar flow-through M^2FCs [25]. This stack offered advantages in device simplicity and compactness. However, uneven flow and reactant distributions to cells remained a problem in their work. They also only studied the case of two cells connected in parallel, and a current loss of 30% was found due to the unequal performance of unit cells in the stack. There have been still some more generalized scaling-out strategies developed based on multiplexing technologies [26, 27]. However, none of these studies does a good job of handling the issue of uniform flow and reactant distributions. Relying on a coupled experimental and computational modeling approach, Ho and Kjeang [27] studied the flow distributions in the asymmetric unilateral and symmetric bilateral multiplexing of M^2FCs and concluded that the symmetric method was preferable in terms of flow distribution uniformity and array performance. However, their conclusion was drawn from an ideal two-cell case by only considering frictional pressure drop, and thus, it has limited applicability to real-world situations where the factors responsible for fluid maldistribution can be far more complex, including the density/viscosity mismatch between two reactant streams, bubble formation, fabrication errors and unbalanced local pressure distribution at the inlet/exit manifolds caused by the specific placement of the inlet/outlet tubes [28-30].

Therefore, the purpose of this study is to develop a more general and reliable M^2FC scaling-out approach that ensures the same working conditions (e.g., flow rates and reactant concentrations) for each individual unit cell. To achieve this goal, a four-cell array was constructed with an integrated fluid circuit, which is designed to provide both uniform flow

distribution and isolation against internal shunt currents in the assembly. The cells in the array are electrically connected in parallel and in series to attain higher currents and voltages, respectively. Through experiments and a shunt current model, the performance and characteristics of the developed array were carefully examined. The parametric dependence of the array performance and further device scalability were also investigated to elucidate the future development of M^2FC scaling-out technologies.

2. Experimental

2.1. Single cell fabrication

The single cell to be scaled out is a T-shaped-counter flow M^2FC similar to the one described in our previous works [31]. Different from the co-flow configuration featuring two aqueous co-laminar reactant streams and electrodes on opposite channel walls parallel to the inter-diffusion zone, the counter-flow one positions the electrodes orthogonal to the mixing interface and operates with a counter-flow of the anode stream relative to the cathode stream before they merge. The cell fabrication and working principles are detailed as follows. As illustrated in the enlarged view of a unit cell in Fig. 1, a T-shaped microfluidic channel was engraved in a poly (methyl methacrylate) (PMMA) substrate to have a width of 1000 μm and a height of 500 μm by carbon dioxide (CO_2) laser cutting (VLS2.30, Universal Laser System Inc.). The T-channel guides the flows of anolyte and catholyte counter to each other before they merge at the T-junction, where an interfacial mixing zone begins to be formed with its width defined under the combined effects of convection and diffusion. The CO_2 laser machining technique was selected here because of its favorable features for future mass production of M^2FCs/M^2FC stacks, including large treatment capacity, high efficiency and low cost. A small hole was punched out at the end of the T-leg to serve as a fluid outlet. Two electrodes (*i.e.,* anode and cathode) were embedded side by side on the bottom of the two

arms of the T-channel. The distance between the two electrodes was set to be 3 mm to create an adequate separation from the interfacial mixing zone and avoid crossover effects. Both the electrodes were in a flow-over planar type and made up of 3.5-mm wide by 2-mm long carbon paper (HCP120, Hesen) with the area inside the channel coated by 2 mg cm^{-2} Pt/C (60 wt.% Pt, Johnson Matthey) as a catalyst. The projected active electrode area in the study is therefore 1 (*W*) × 2 (*L*) mm^2. The remaining uncatalyzed part of the electrodes serves as electrode terminals to provide electrical connection to an external circuit. It is worth noting that the present study mainly focuses on the development of a general and reliable M^2FC scaling-out method. It is not within our scope to address any single cell issues such as cell durability, geometry optimization and electrode activity, which are also hot research topics. Therefore, the design, materials and chemistry of the present single cell were arbitrarily chosen from the existing technologies, and they do not represent optimal conditions. The scaling-out strategy described in this work is equally applicable to other M^2FC architectures.

2.2. Cell array design and fabrication

The M^2FC array consisted of four unit cells electrically connected in parallel or in series. The corresponding assembly schemes are shown in Fig. 1(a1) and Fig. 1(a2). Fig. 1(b) provides a photograph of the four-cell array prototype. It can be seen from the figures that both assemblies contain three layers of PMMA plates fabricated with CO_2 laser cutting. The top layer contains two inlets for delivering anolyte and catholyte, respectively. In addition, eight small orifices (2.5 (*W*) × 2 (*L*) mm^2 each) opened to the uncatalyzed part of the cell electrodes were also cut out in the top layer. Graphite ink with good electronic conductivity (DB5018, Double-bond Chemical) was used to fill up the orifices to lead the electrodes out for further cell connections. An electrical connection between unit cells was created on the outer surface of the top layer with silver ink by hand lining. Both the graphite and silver inks

were cured in an oven at 343 K for 2 h. Two separate pieces of copper foil were separately attached to the two ends of the connection circuit. The copper pieces act as positive and negative terminals of the array and connect to an external load.

In the middle layer, four repeated unit cells were fabricated with their channels fluidically connected via two multi-branch fluid distributors engraved in the same plate. To balance the pressures between cells and minimize bypass current, a serpentine configuration that generates high-enough fluidic and ionic resistances was applied to the distribution branches. The total length of each serpentine branch was set to 281.4 mm. According to our scanning electron microscopy observation (SEM, Hitachi S-3400) in Fig. 1(c), the fabricated branches have a triangular cross section with a height of 313 μm and a base of 313 μm.

The bottom layer is mainly designed for exhaust fluid collection. The present study employed two different collection strategies under different cell connections. For the parallel array, as shown in Fig. 1(a1), a collection manifold composed of four straight branches (1 (*W*) × 0.5 (*H*) mm^2) was formed at the bottom plate to collect the exhaust fluids from each unit cell and direct them out of the assembly via an outlet located at the top layer. However, the same strategy may cause severe shunt current loss in the series-connected case as will be discussed later. Therefore, for the series array in Fig. 1(a2), four polyethylene tubes (length = 3 mm, i.d. = 1.57 mm) were glued to each cell outlet to provide separate passages to the fluids existing from different cells. The fluids were then collected in a 15-mm-deep reservoir appended to the middle layer and drained out from the device via the hole at the bottom of the reservoir.

The multilayer assembly was bonded together by hot pressing (Elcometer 8400) at 6.5 kPa and 363 K for 30 min. Prior to our experiments, a leakage test of the assembly was performed by flowing deionized water through the device for several minutes.

2.3. Chemical reagents and instrumentation

Interfacial species mixing in the T-shaped cell channels was visualized by feeding the two inlets of the array with 0.5 M sodium hydroxide (AR, Uni-chem) and 0.1 wt.% phenolphthalein (AR, Sigma-Aldrich) dissolved in 60% (v/v) ethanol (Merck). The mixing of hydroxides and phenolphthalein triggers a color change in the solution from transparent to fuchsia. The fuel cell performance was tested using an anolyte composed of 0.5 M formic acid (Sigma-Aldrich) in 0.5 M H_2SO_4 (Sigma-Aldrich) and a catholyte composed of 0.01 M H_2O_2 (Sigma-Aldrich) in 0.5 M H_2SO_4 (Sigma-Aldrich). This combination is one of the most commonly used reactant combinations in fuel cells, and its related electrode chemistries at 298 K are [32, 33]

Anode: $HCOOH \rightarrow CO_2 + 2H^+ + 2e^-$ $E^0 = -0.199$ V vs SHE (R1)

Cathode: $H_2O_2 + 2H^+ + 2e^- \rightarrow 2H_2O$ $E^0 = 1.776$ V vs SHE (R2)

$H_2O_2 \rightarrow O_2 + 2H^+ + 2e^-$ $E^0 = 0.682$ V vs SHE (R3)

$O_2 + 4H^+ + 4e^- \rightarrow 2H_2O$ $E^0 = 1.229$ V vs SHE (R4)

According to the above, the cathode process involves both reactions of direct hydrogen peroxide reduction and indirect oxygen reduction following hydrogen peroxide decomposition (as shown in Eqs. (R2)~(R4)). Thus, the cathode potential at open circuit is a mixed potential, which was reported to occur around 0.85 V on Pt in acid solution [33]. Electricity is generated when the produced electrons at the anode pass through an external circuit to the cathode. Meanwhile, protons as the charge carrier migrate from the anode to the cathode to close the internal circuit. All aqueous solutions in the experiments were prepared with Milli-Q water (18 MΩ, Barnstead Nanopure). The fluid streams were supplied to the cell at controlled flow rates using a dual syringe pump (LSP02-1B, Longer Pump).

Prior to electrochemical tests, the flow distributions in the array were first examined. The flow rate for each unit cell was determined by collecting and weighing the fluid exiting from

the cell over a certain time span with an electronic balance (AEG-120, Shimadzu). To reduce experimental errors, all measurements were repeated five times.

The cell polarization was measured under ambient conditions using a CHI 660E electrochemistry workstation by chronoamperometry technique under potentiostatic control. The cell potential was stepped from 0.0 V to the open circuit voltage in 0.1 V increments with its discharge current recorded at each potential for 300 s. The recorded current was then averaged over the last 60 s to ensure a steady-state operation. It is noted that thermal effects are not considered in this work as the temperature variation during the cell operation is negligible due to the small discharge currents along with the heat removal by the flowing electrolyte. According to our previous study [34], even at a current density of 500 mA cm^{-2}, the temperature variation inside a M^2FC is still below 1 K. However, when considering further scale-out of the cell number and more practical large-power operation, thermal effects are likely to become remarkable. Excessive or uneven temperature rise in a cell or cell array can significantly affect both its short and long-term performances through altering electrode kinetics, changing electrolyte properties and accelerating material degradation [35-37]. Without a proper control, severe problems such as local hot spots, thermal runaway and heat stress may occur to deteriorate the system output and life-span [38]. Thus, an understanding of the heat transfer and management issues in the M^2FC array is of great importance for its further development, which requires systematic study yet is beyond our current scope.

As the required parameters for the model simulation, the electrical conductivities of electrolyte streams were obtained using a conductivity meter (Mettler Toledo, model SevenMulti).

3. Shunt current model

It is noteworthy that the electrolyte-filled multi-branch flow distributors in the present

array design do not only provide necessary fluidic connections but also undesired electric connections among unit cells. Because of inter-cell potential gradients, the ionic currents generated by electrode processes are driven through these conductive fluid paths to form shunt currents. The shunt currents short circuit each cell in the array and may cause severe energy and power losses as previously observed in the stacks of flow batteries and alkaline fuel cells [39-41]. To evaluate the shunt current impacts in our array design, a shunt current model was developed based on a circuit analog approach. The circuit analog approach is a well-established technique and has been widely adopted in studies for the prediction of the bypassing flow of current in flow battery/fuel cell stacks [42-44]. The general assumptions applied to the model development include the following: (i) unit cells in the array are treated as voltage sources with their polarization behaviors describable using a simple linear relationship at each discharge point; (ii) the electrolyte-filled channels are represented by resistors, and resistors placed in equivalent places are considered to be identical; (iii) the electrolyte in the channels is very well mixed such that the solution properties are uniform throughout; (iv) electrodes and the corresponding electrical connections provide no resistance to current flow.

3.1. Series connection

The analog circuit of the array consisting of N unit cells electrically connected in series is presented in Fig. 2(a). The components included in the circuit are as follows: R_n, internal cell resistance; V_0, open-circuit cell voltage; R_a and R_c, distribution branch resistance for the anolyte and catholyte, respectively; r_a and r_c, distribution manifold resistance between cells for the anolyte and catholyte, respectively. No fluid collection components are taken into account in the circuit as they do not form any closed path for current flow as indicated in Fig. 1(a2). A transformation of the circuit into a more intuitive current flow-based form is given in

the lower part of Fig. 2(a). The discharge current of the array is denoted by I_T.

Application of Kirchhoff's first and second laws to the circuit results in the below system of five linear algebraic equations:

$$i_{c,n+1} - i_{c,n} - I_{c,\,n+1} = 0 \tag{1}$$

$$i_{a,n+1} - i_{a,n} - I_{a,\,n+1} = 0 \tag{2}$$

$$I_{n+1} - I_n + I_{c,\,n+1} + I_{a,\,n+1} = 0 \tag{3}$$

$$V_0 - R_a \times (I_{a,\,n+1} - I_{a,\,n}) + r_a \times i_a - R_n \times I_n = 0 \tag{4}$$

$$V_0 - R_c \times (I_{c,\,n+1} - I_{c,\,n}) + r_c \times i_c - R_n \times I_n = 0 \tag{5}$$

Additional equations obtained with the first cell and the *N*th cell in the array are:

$$I_{a,\,1} = i_{a,\,1} \tag{6}$$

$$I_1 = I_T - I_{a,\,1} \tag{7}$$

$$I_{c,\,N+1} = i_{c,\,N} \tag{8}$$

$$I_N = I_T + I_{c,\,N+1} \tag{9}$$

In the above equations, the resistances R_a, R_c, r_a and r_c can be evaluated by [45]:

$$R_i = \frac{1}{\kappa_i} \times \frac{L_i}{A_i} \tag{10}$$

where the electrolyte conductivities κ_i, the channel lengths L_i, and the cross-sectional areas of channels A_i are all measurable in experiments.

Ideally, all unit cells in the array should work under the same conditions and exhibit the same polarization characteristics. Therefore, they share the same intrinsic resistance, which can be obtained by fitting the measured voltage and current data of a single cell point by point using the following linear relation [46]:

$$\bar{R} = \frac{V_0 - V}{I} \tag{11}$$

where the cell resistance, $\bar{R}$, contains information about the electrode/electrolyte ohmic resistances and mass transport losses as well as activation losses. However, the ideal state of

same cell performance is hardly achieved in practice as a consequence of the factors introduced before. To account for the discrepancy of the behavior of each practical cell from the ideal value, the corrected internal resistances are calculated by

$$R_n = \overline{R} \times (C_n)^{-1} \tag{12}$$

where C_n is the correction factor, the values of which obey a normal distribution with a mean of 1 and a standard deviation of σ (*i.e.*, $C_n \sim \mathcal{N}(1, \sigma^2)$). It is reasonable to regard the parameter σ as an inconsistency coefficient as the dispersion of C_n values, and thereby cell behavior consistency, is determined by the value of σ. A smaller σ value indicates more consistent polarization behavior of each unit cell and vice versa.

Because of the series cell connection, the overall output voltage of the device is the algebraic sum of individual cell voltages, *i.e.*,

$$V_T = \sum_{n=1}^{N} V_n \tag{13}$$

where the practical voltage of each unit cell is computed using Eq. (14) with a solved current value from the shunt current model.

$$V_n = V_0 - I_n \times R_n \tag{14}$$

The scaling-out efficiency of the array in this study is expressed in terms of peak power by

$$\eta = \frac{P_T^{\max}}{N \times P_n^{\max}} = \frac{V_T|_{P_T=P_T^{\max}} \times I_T|_{P_T=P_T^{\max}}}{N \times V|_{P=P^{\max}} \times I|_{P=P^{\max}}} \tag{15}$$

3.2. Parallel connection

Fig. 2(b) shows the analog circuit of the array consisting of N unit cells electrically connected in parallel. Apart from the components described in the preceding model, resistances of collection branches (R_o) and manifolds (r_o) are also involved in this circuit. However, according to the circuit, the bypass current in the branches and manifolds can be negligible as the electronic connections between cells offer a preferable path for current flow.

The circuit for the array performance modeling is therefore further simplified as shown in the lower part of the figure. The following simple relationship based on Ohm's law is used to calculate the array polarization:

$$I_T = \sum_{n=1}^{N} \frac{V_0 - V_T}{R_n} \tag{16}$$

where the open circuit voltage V_0 is measured from the experiments, and the cell internal resistance R_n is corrected from Eq. (12) just as in the preceding model.

3.3. Input parameters and solution procedure

The input parameters to the model for the base case conditions (*i.e.*, experimental conditions) are listed in Table 1. The values of the correction factor C_n were randomly generated using MATLAB. For each given σ, five sets of C_n values were created and used in the simulation to minimize the effect of C_n values on modeling results. The model was solved using the commercial electronic circuit simulation software PSPICE.

4. Results and discussion

4.1. Flow and reactant distributions in the four-cell array

A uniform flow distribution from the manifolds to each unit cell is essential for reliable, controllable and efficient M^2FC array or stack operations. However, due to the various aforesaid uncontrollable factors, pressure/flow resistance imbalances between cells are inevitably present in practice and pose a great challenge to M^2FC scale-out. In this study, serpentine-branch distributors were integrated into the array design to address this problem.

Fig. 3(a) compares the flow distributions in the present four-cell array and an array incorporating conventional straight-branch distributors at an overall flow rate of 400 μL min^{-1}. It is obvious that the present strategy offers much better flow distribution uniformity. By adopting the serpentine distribution passages, the maximum flow rate discrepancy of the four

unit cells in this study drops to 7% of the all-cell-averaged flow rate. Moreover, the rate's associated small error bars (within ±0.15 μL min^{-1}) indicate a good reproducibility of the data. In contrast, for the array using straight-branch distributors, the maximum cell flow rate is almost 7 times that of the minimum cell flow rate, as shown in Fig. 3(a). Because of the unpredictable flow resistance fluctuations inside the microchannels, the measurements with straight branches are hardly repeatable as reflected by their large error bars. In some measurements, even worse, flow reversal occurred in the cell channels. The above-described huge discrepancy and variation in cell flow rates are detrimental to array/stack performance and can even cause device failures.

We further examined the effect of flow rate on the flow distribution uniformity in our array design. The relative standard deviation (RSD) of all five independent measurements at four cells (*i.e.*, the ratio of the standard deviation to the mean) was adopted as an indicator of the flow distribution uniformity. As shown in the inset of Fig. 3(a), the RSD value decreases from 13.6% to 1.74% as the overall flow rate increases from 4 μL min^{-1} to 4000 μL min^{-1}, indicating more uniform flow distributions at higher flow rates.

The improved flow distribution uniformity with the serpentine branches can be explained through an electronic-hydraulic analogy [47-49] shown in Fig. 3(b). For simplicity, Fig. 3(b) only considers a two-cell case with half of the device geometry in view of the symmetry of the T-junctions. The following relationship is therefore derived from the analogy:

$$\Delta Q_{12} = Q_1 - Q_2 = \left(p_{in} - p_{out}\right)\left(\frac{1}{\tau_{S1} + \tau_{T1}} - \frac{1}{\tau_{S2} + \tau_{T2}}\right) \tag{17}$$

where $Q_{1,2}$ denotes the flow rate of each individual stream; p_{in} and p_{out} denote the pressure at the inlet and the outlet of the array; τ_{S} denotes the flow resistance created by each distribution branch; τ_{T} denotes the flow resistance created by the remaining part of the fluid passage for each cell. According to Eq. (17), an identical flow rate to each cell ($\Delta Q_{12} = 0$) is guaranteed upon the condition of equal flow resistances along different cell passages, *i.e.*, $\tau_{\text{S1}} + \tau_{\text{T1}} = \tau_{\text{S2}}$

+ τ_{T2}, which are practically unachievable as discussed. Here, the incorporation of the serpentine branches generates a very large value of τ_S due to the long and narrow nature of serpentine configuration ($\tau \propto f(L, A^{-1})$). This helps diminish the effect of the flow resistance imbalances among cells and consequently uniformize flow distributions. In contrast, with regular straight channels, the flow resistances of the feeds to the different unit cells are much smaller and the effect of flow resistance differences becomes significant. Despite the large flow resistance of serpentine passages, it is worth noting that the total pump power consumption in the present design will not increase linearly with the cell number (*i.e.*, the number of serpentine passages) because of the parallel fluidic connections between cells. According to a correlation derived from Hagen-Poiseuille's law [49],

$$\tau = \frac{\mu L \chi}{2\pi A} \tag{18}$$

The hydraulic resistance of each individual serpentine channel in the array is estimated to be 8.2×10^{12} Pa s m^{-3}. At 100 μL min^{-1}, its corresponding pressure drop is 1.4×10^{4} Pa, and its pumping power is 22.8 μW, which can be over two orders of magnitude lower than the unit-cell power output from state-of-the art M^{2}FC technologies [13, 15, 23].

Fig. 3(c) visualizes the interfacial species mixing in each unit cell of the array at different flow rates. In this figure, it can be seen that the mixing interfaces in all of the cells are kept aligned to the center of the T-channels because of well-balanced flow rates between the counter-flowing streams. The widths of the mixing regions are measured for the four cells at a point half way down the T-leg of the cell channel with RSDs of the four values calculated to be 3.1%, 2.7% and 1.9% at flow rates of 4 μL min^{-1}, 400 μL min^{-1} and 2000 μL min^{-1}, respectively, which are quite small and again confirm the reasonable flow distribution uniformity in the present array design.

For the remainder of the discussion, a moderate flow rate of 400 μL min^{-1} (*i.e.*, 100 μL min^{-1} per single cell) is applied to the array unless otherwise specified.

4.2. Electrochemical performance of the four-cell array

The polarization and power curves of the four-cell array are plotted in Fig. 4 against single cell performance. The four individual cells in the array are connected in parallel and series to increase the current and voltage. During the parallel connection, the array delivers a maximum current of 1133.6 μA and a maximum power of 265.8 μW, which are 3.98 and 3.72 times that of the single cell compared in Fig. 4(a), respectively. Whereas in Fig. 4(b), it can be observed that the connection of the four cells in series results in 3.86-fold increases of open circuit voltage (OCV) (2.89 V vs. 0.75 V for the single cell) and 3.3-fold increase of peak power (235.8 μW vs. 71.4 μW for the single cell). The corresponding scaling-out efficiencies are 93% and 82% for the parallel and series connection, respectively. The non-unity scaling-out efficiency during the parallel connection is likely to be caused by slight differences in cell performances, as there is no shunt current loss in the parallel array. The relatively lower scaling-out efficiency of the series array is attributed to additional losses induced by bypass current in the manifolds and branches, the effects of which will be analyzed in detail in the subsequent sections using a shunt current model. It also can be noted from both Fig. 4(a) and Fig. 4(b) that the cell operation never reaches limiting current region where the value of current stops growing with voltage drop and cell performance is completely limited by mass transport. According to the formulas given by previous studies [50, 51], the limiting current for the present single cell operation are calculated to be 807 μA and 357 μA at the anode and the cathode, respectively, which are well above the present maximum current of 285 μA.

In addition, Fig. 4 compares the measured polarization curves with the simulated results from the shunt current model. Assuming an σ value of 0.25, the simulated curves display good agreement with the experimental data, indicating the validity of the model.

4.3. Ionic resistances of branches and manifolds and their effects

In addition to flow resistance, the present serpentine passages also offer a much higher ionic resistance than straight passages as indicated in Eq. (10). The influence of the branch ionic resistance on the array performance was investigated based on the shunt current model. Because the output of the parallel array is not related to the branch resistance according to the analog circuit in Fig. 2(b), only the series-connected case is considered here. Assuming a perfect cell consistency (*i.e.*, σ = 0), performance curves of the four-cell array with serpentine-branch and straight-branch distributors are modeled and compared in Fig. 5(a). According to the modeling results shown in Fig. 5(a), the incorporation of serpentine channels increases the OCV and peak power of the device by 2.6 and three times, respectively, compared with the device employing straight-branch distributors. This great performance enhancement is attributable to the largely increased ionic resistances with serpentine branches, which can be two orders of magnitude higher than the straight branches as estimated by Eq. (10). The large ionic resistances inhibit currents from passing through these distribution branches back to the manifolds. In comparison, shorter and wider straight-channels that create much less ionic resistances allow greater bypass currents, reducing the overall array output. Fig. 5(b) plots the scaling-out efficiency as a function of the branch resistance. In the figure, the scaling-out efficiency rapidly increases with increasing branch resistance at first and then tends to reach a plateau at a resistance of 50 kΩ. It is noteworthy that the serpentine-branch resistance in our study is approximately 233 kΩ and well beyond the "plateau" threshold.

To gain more insights, shunt current distributions under different branch resistances are compared in Fig. 5(c) at a constant discharge current. For all three resistance values listed in Fig. 5(c), their shunt current distributions exhibit a similar profile. The shunt current in the

branch has peaks in absolute value at the two ends of the array (*i.e.*, cell 1 and 4) and decreased values toward the center (*i.e.*, cell 2 and 3), whereas the maximum shunt current in manifold occurs at the array center. Not surprisingly, both shunt currents in the manifold and branch decrease with the increase of the branch resistance. In Fig. 5(d), the corresponding distributions of individual single cell voltage and internal current are demonstrated. For different resistance values, it can be seen that the internal current composed of the current transmitted from the former cell and branch currents (refer to Eq. (3)) reaches its maximum values at the array center. Accordingly, the central cells (*i.e.*, cell 2 and 3) work at much lower voltages. The increase of the branch resistance is found to suppress the internal currents and thus increase the array output by flattening the voltage distribution curve.

As part of the connection fluidic circuit, knowing the manifold resistance effect on the array output has value. As shown in Fig. 5(e) and Fig. 5(f), doubling the manifold resistance results in the same but insignificant variation of shunt currents, cell voltage and internal current in the array compared with doubling the branch resistance. This can be explained by the fact that the manifold resistance is much smaller than the branch resistance in the present fluidic circuit design.

4.4. The effect of behavior inconsistency of unit cells

Although nearly uniform flow and reactant distributions are ensured in the study with the serpentine-branch distributors, differences in cell behaviors cannot be eradicated because of the presence of fabrication/assembly errors. Particularly for M^2FCs, their small dimensions make their discharge characteristics highly sensitive to these errors. Thus, it is still necessary to study the effect of cell inconsistency on our array performance.

For different degrees of cell inconsistency, the polarization and power curves of the array with four cells connected in series are simulated as in Fig. 6(a). When cell inconsistency

increases, a notable decrease of the array performance is observed. The series array performance was found to be affected by the inconsistency coefficient in two ways. First, the change of the inconsistency coefficient alters the shunt current distribution and thereby the array output through changing cell internal resistance. However, this performance change is insignificant as a consequence of the very high ionic resistances in the branches in our array design. Second, non-zero inconsistency coefficients result in the appearance of disadvantaged cells in the array (*i.e.*, cells at $C_n < 1$). Compared with an ideal cell at $C_n = 1$, these disadvantaged cells undergo more severe polarization under the same discharge current and fail prematurely due to their faster voltage drop with current. Similar to series battery packs, these cells act as a "short board" and drag down the overall array output. The increase of the inconsistency coefficient can worsen the performance of disadvantaged cells and thus intensify the decay of the array performance. Because of the absence of shunt current, for the parallel connection, the array output is a simple summation of output of each unit cell, which can also deviate from its expected value as a result of inconsistent cell behaviors. This, however, is not reflected in the present model.

Fig. 6(b) shows the power efficiency of the series array as a function of the inconsistency coefficient at different discharge currents. As expected, the power efficiency drops faster at larger currents because of the premature failure of disadvantaged cells. With an inconsistency coefficient greater than 0.44, the power efficiency becomes zero at the discharge current of 247.2 μA, indicating that the maximum achievable current under this circumstance is 247.2 μA. The above results suggest that high-precision microfabrication techniques that enable better cell consistency are preferable for the present array design.

4.5. The effect of the number of cells in series

The array performance variation with the number of cells in series was analyzed

considering the presence of shunt current. Fig. 7(a) and Fig. 7(b) compare the distributions of shunt current, internal current and cell voltage in the series array containing four cells and eight cells. The increase of cell number from four to eight can significantly intensify the shunt currents and thereby lower the cell voltages. As a result, the scaling-out efficiency gradually drops with cell number as seen in Fig. 7(c). To maintain a reasonable scaling-out efficiency above 75%, the present array has to be limited to 16 cells in series.

For the purpose of enhancing the device expandability, the following two methods were attempted: (i) further increasing the branch ionic resistance and (ii) replacing the present unit cell with cells having better performance. As demonstrated in Fig. 7(c), a ten-fold increase in branch resistance almost triples the scaling-out efficiency at 100 cells. Alternatively, a similar extent in the efficiency improvement is observed in Fig. 7(e) upon the reduction of the cell intrinsic resistance by ten times (equivalent to a ten-fold performance improvement). Through either of the above methods, the array can be incremented to 50 cells in series with over 75% efficiency. Distributions of shunt current and cell voltage in the 100-cell array with the decoupled branch resistance and cell performance are further examined in Fig. 7(d) and Fig. 7(f), respectively. It can be seen from Fig. 7(d) that an increased branch resistance boosts the scaling-out efficiency by reducing shunt current and alleviating the voltage drop at the central cells. However, in contrast to the case of a decupled branch resistance, the efficiency retrieval with enhanced cell performance is accomplished because of the reduced ratio of shunt current to internal current, as indicated in Fig. 7(f).

In practice, higher branch resistances are readily attainable by increasing the channel length and shrinking the cross-sectional area. On the other hand, the unit cell performance can be enhanced with improved reactant flow-fields, electrode structures and catalysts. Although the enhancement of single M^2FC performance is not within the scope of this study, it is noted that many single cell studies have reported M^2FC performance ten-fold that of the

present study through employing certain combinations of fuel/oxidant, advanced catalysts or cell designs [13, 15, 52].

5. Conclusions

In this paper, a scaling-out strategy was presented for general M^2FC applications. To demonstrate its feasibility, a four-cell array was constructed and tested using formic acid as a fuel and hydrogen peroxide as an oxidant. The unit cells in the array are fluidically connected in parallel with a well-designed fluidic circuit consisting of serpentine channels. Thanks to the high fluidic and ionic resistances of the serpentine channel, the present M^2FC array has advantages over the previous prototypes in flow distribution uniformity and shunt current suppression. The electrical connection of the four unit cells in parallel and in series increases the array current and voltage by 3.98 and 3.86 times, respectively, and thereby increases the power output. The corresponding scaling-out efficiencies in terms of peak power are 93% and 82% for the parallel and series connection, respectively. Considering that shunt current can be the major cause of the efficiency deterioration, a shunt current model is developed based on the circuit analog approach to understand performance loss and parametric effects in our array design. The model is validated against the experimental data. The modeling results indicated that the performance of the present array design can be further improved by increasing cell consistency. Moreover, further scaling out of the present array is still feasible as long as the branch resistance or the performance of the unit cell is sufficiently high.

Acknowledgments

The research work presented in this paper was supported by the CRCG of the University of Hong Kong, the National Basic Research Program of China (973 Program) (2014CB748500), Shanghai Pujiang Program (12PJ1402100), the Fundamental Research Funds for the Central

Universities (WG1214029) and the Young Teachers Program of Universities in Shanghai (ZZHLG12012).

References

[1] F. R. Brushett, R. S. Jayashree, W. P. Zhou, P. J. A. Kenis, Investigation of fuel and media flexible laminar flow-based fuel cells, Electrochim. Acta 54 (2009) 7099.

[2] E. R. Choban, L. J. Markoski, A. Wieckowski, P. J. A. Kenis, Microfluidic fuel cell based on laminar flow, J. Power Sources 128 (2004) 54.

[3] E. R. Choban, J. S. Spendelow, L. Gancs, A. Wieckowski, P. J. A. Kenis, Membraneless laminar flow-based micro fuel cells operating in alkaline, acidic, and acidic/alkaline media, Electrochim. Acta 50 (2005) 5390.

[4] R. Ferrigno, A. D. Stroock, T. D. Clark, M. Mayer, G. M. Whitesides, Membraneless vanadium redox fuel cell using laminar flow, J. Am. Chem. Soc. 124 (2002) 12930.

[5] A. S. Hollinger, R. J. Maloney, R. S. Jayashree, D. Natarajan, L. J. Markoski, P. J. A. Kenis, Nanoporous separator and low fuel concentration to minimize crossover in direct methanol laminar flow fuel cells, J. Power Sources 195 (2010) 3523.

[6] R. S. Jayashree, S. K. Yoon, F. R. Brushett, P. O. Lopez-Montesinos, D. Natarajan, L. J. Markoski, P. J. A. Kenis, On the performance of membraneless laminar flow-based fuel cells, J. Power Sources 195 (2010) 3569.

[7] E. Kjeang, B. T. Proctor, A. G. Brolo, D. A. Harrington, N. Djilali, D. Sinton, High-performance microfluidic vanadium redox fuel cell, Electrochim. Acta 52 (2007) 4942.

[8] H. B. Park, D. H. Ahmed, K. H. Lee, H. J. Sung, An H-shaped design for membraneless micro fuel cells, Electrochim. Acta 54 (2009) 4416.

[9] K. S. Salloum, J. R. Hayes, C. A. Friesen, J. D. Posner, Sequential flow membraneless microfluidic fuel cell with porous electrodes, J. Power Sources 180 (2008) 243.

[10] K. S. Salloum, J. D. Posner, Counter flow membraneless microfluidic fuel cell, J. Power Sources 195 (2010) 6941.

[11] A. S. Hollinger, P. J. A. Kenis, Manufacturing all-polymer laminar flow-based fuel cells, J. Power Sources 240 (2013) 486.

[12] P. O. López-Montesinos, N. Yossakda, A. Schmidt, F. R. Brushett, W. E. Pelton, P. J. A. Kenis, Design, fabrication, and characterization of a planar, silicon-based, monolithically integrated micro laminar flow fuel cell with a bridge-shaped microchannel cross-section, J. Power Sources 196 (2011) 4638.

[13] W. A. Braff, M. Z. Bazant, C. R. Buie, Membrane-less hydrogen bromine flow battery, Nat Commun 4 (2013) 2346.

[14] E. Kjeang, R. Michel, D. A. Harrington, D. Sinton, N. Djilali, An alkaline microfluidic fuel cell based on formate and hypochlorite bleach, Electrochim. Acta 54 (2008) 698.

[15] N. D. Mota, D. A. Finkelstein, J. D. Kirtland, C. A. Rodriguez, A. D. Stroock, H. D. Abruña, Membraneless, room-temperature, direct borohydride/cerium fuel cell with power density of over 0.25 W/cm^2, J. Am. Chem. Soc. 134 (2012) 6076.

[16] F. R. Brushett, H. T. Duong, W. J. D. Ng, R. L. Behrens, A. Wieckowski, P. J. A. Kenis, Investigation of Pt, Pt_3Co, and Pt_3Co/Mo cathodes for the ORR in a microfluidic H_2/O_2 fuel cell, J. Electrochem. Soc. 157 (2010) B837.

[17] F. R. Brushett, M. S. Thorum, N. S. Lioutas, M. S. Naughton, C. Tornow, H. R. M. Jhong, A. A. Gewirth, P. J. A. Kenis, A carbon-supported copper complex of 3,5-diamino-1,2,4-triazole as a cathode catalyst for alkaline fuel cell applications, J. Am. Chem. Soc. 132 (2010) 12185.

[18] R. S. Jayashree, J. S. Spendelow, J. Yeom, C. Rastogi, M. A. Shannon, P. J. A. Kenis, Characterization and application of electrodeposited Pt, Pt/Pd, and Pd catalyst structures for direct formic acid micro fuel cells, Electrochim. Acta 50 (2005) 4674.

[19] S. A. Mousavi Shaegh, N. T. Nguyen, S. M. Mousavi Ehteshami, S. H. Chan, A membraneless hydrogen peroxide fuel cell using Prussian Blue as cathode material, Energy & Environmental Science, 5 (2012) 8225.

[20] D. T. Whipple, R. S. Jayashree, D. Egas, N. Alonso-Vante, P. J. A. Kenis, Ruthenium cluster-like chalcogenide as a methanol tolerant cathode catalyst in air-breathing laminar flow fuel cells, Electrochim. Acta 54 (2009) 4384.

[21] E. Kjeang, N. Djilali, D. Sinton, Microfluidic fuel cells: A review, J. Power Sources 186 (2009) 353.

[22] S. A. M. Shaegh, N. T. Nguyen, S. H. Chan, A review on membraneless laminar flow-based fuel cells, Int J Hydrogen Energ 36 (2011) 5675.

[23] M. R. Thorson, F. R. Brushett, C. J. Timberg, P. J. A. Kenis, Design rules for electrode arrangement in an air-breathing alkaline direct methanol laminar flow fuel cell, J. Power Sources 218 (2012) 28.

[24] K. S. Salloum, J. D. Posner, A membraneless microfluidic fuel cell stack, J. Power Sources 196 (2011) 1229.

[25] S. Moore, D. Sinton, D. Erickson, A plate-frame flow-through microfluidic fuel cell stack, J. Power Sources 196 (2011) 9481.

[26] J. L. Cohen, D. A. Westly, A. Pechenik, H. D. Abruña, Fabrication and preliminary testing of a planar membraneless microchannel fuel cell, J. Power Sources 139 (2005) 96.

[27] B. Ho, E. Kjeang, Planar multiplexing of microfluidic fuel cells, J. Fluids Eng. 135 (2013) 021304.

[28] D. D. Meng, C. J. Kim, An active micro-direct methanol fuel cell with self-circulation of

fuel and built-in removal of CO_2 bubbles, J. Power Sources 194 (2009) 445.

[29] S.G. Kandlikar, Z. Lu, W.E. Domigan, A.D. White, M.W. Benedict, Measurement of flow maldistribution in parallel channels and its application to ex-situ and in-situ experiments in PEMFC water management studies, Int. J. Heat Mass Transfer 52 (2009) 1741.

[30] J. Xuan, M. K. H. Leung, D. Y. C. Leung, M. Ni, Density-induced asymmetric pair of Dean vortices and its effects on mass transfer in a curved microchannel with two-layer laminar stream, Chem. Eng. J. 171 (2011) 216.

[31] Y. Shen, J. Xuan, H. Wang, D. Y. C. Leung, M. K. H Leung, S. Gu, H. Xu, L. Zhang, A self-pumping microfluidic fuel cell based on hydrostatic principles, The 5th International Conference on Applied Energy, Pretoria, South Africa, 2013.

[32] A. Li, S. H. Chan, N. T. Nguyen, A laser-micromachined polymeric membraneless fuel cell, J. Micromech. Microeng. 17 (2007) 1107.

[33] E. Kjeang, A. G. Brolo, D. A. Harrington, N. Djilali, D. Sinton, Hydrogen peroxide as an oxidant for microfluidic fuel cells, J. Electrochem. Soc. 154 (2007) B1220.

[34] J. Xuan, D. Y. C. Leung, M. K. H. Leung, M. Ni, H. Wang, A computational study of bifunctional oxygen electrode in air-breathing reversible microfluidic fuel cells, Int. J. Hydrogen Energy 36 (2011) 9231.

[35] S.S. Mahapatra, A. Dutta, J. Datta, Temperature effect on the electrode kinetics of ethanol oxidation on Pd modified Pt electrodes and the estimation of intermediates formed in alkali medium, Electrochim. Acta 55 (2010) 9097.

[36] J. Barthel, The temperature dependence of the properties of electrolyte solutions. I. A semi-phenomenological approach to an electrolyte theory including short range forces, Berichte der Bunsengesellschaft für physikalische Chemie 83 (1979) 252.

[37] Y. Shao, G. Yin, Y. Gao, Understanding and approaches for the durability issues of Pt-based catalysts for PEM fuel cell, J. Power Sources 171 (2007) 558.

[38] Z. Rao, S. Wang, A review of power battery thermal energy management, Renew. Sust. Energ. Rev. 15 (2011) 4554.

[39] P. Zhao, H. Zhang, H. Zhou, J. Chen, S. Gao, B. Yi, Characteristics and performance of 10 kW class all-vanadium redox-flow battery stack, J. Power Sources 162 (2006) 1416.

[40] G. Zhou, L. Chen, J. P. Seaba, CFD prediction of shunt currents present in alkaline fuel cells, J. Power Sources 196 (2011) 8180.

[41] P. Leung, X. Li, C. P. de León, L. Berlouis, C. T. J. Low, F. C. Walsh, Progress in redox flow batteries, remaining challenges and their applications in energy storage, RSC Adv. 2 (2012) 10125.

[42] H. S. Burney, R. E. White, Predicting shunt currents in stacks of bipolar plate cells with conducting manifolds, J. Electrochem. Soc. 135 (1988) 1609.

[43] F. Xing, H. Zhang, X. Ma, Shunt current loss of the vanadium redox flow battery, J. Power Sources 196 (2011) 10753.

[44] A. Tang, J. McCann, J. Bao, M. Skyllas-Kazacos, Investigation of the effect of shunt current on battery efficiency and stack temperature in vanadium redox flow battery, J Power Sources 242 (2013) 349.

[45] G. Codina, A. Aldaz, Scale-up studies of an Fe/Cr redox flow battery based on shunt current analysis, J. Appl. Electrochem. 22 (1992) 668.

[46] M. S. Naughton, A. A. Moradia, P. J. A. Kenis, Quantitative analysis of single-electrode plots to understand in-situ behavior of individual electrodes, J. Electrochem. Soc. 159 (2012) B761.

[47] N. L. Jeon, S. K. W. Dertinger, D. T. Chiu, I. S. Choi, A. D. Stroock, G. M. Whitesides, Generation of solution and surface gradients using microfluidic systems, Langmuir 16 (2000) 8311.

[48] C. Kim, K. Lee, J. H. Kim, K. S. Shin, K.J. Lee, T. S. Kim, J. Y. Kang, A serial dilution

microfluidic device using a ladder network generating logarithmic or linear concentrations, Lab Chip 8 (2008) 473.

[49] K.W. Oh, K. Lee, B. Ahn, E. P. Furlani, Design of pressure-driven microfluidic networks using electric circuit analogy, Lab Chip 12 (2012) 515.

[50] E. Kjeang, B. Roesch, J. McKechnie, D. A. Harrington, N. Djilali, D. Sinton, Integrated electrochemical velocimetry for microfluidic devices, Microfluid Nanofluid 3 (2007) 403.

[51] J. Xuan, D. Y. C. Leung, M. K. H. Leung, H. Wang, M. Ni, Chaotic flow-based fuel cell built on counter-flow microfluidic network: Predicting the over-limiting current behavior, J. Power Sources 196 (2011) 9391.

[52] R. S. Jayashree, L. Gancs, E. R. Choban, A. Primak, D. Natarajan, L. J. Markoski, P. J. A. Kenis, Air-breathing laminar flow-based microfluidic fuel cell, J. Am. Chem. Soc. 127 (2005) 16758.

Nomenclature

A	cross-sectional area (m^2)
C	correction factor
I	current (A)
i	current in manifold (A)
L	channel length (m)
N	number of cells in array
P	power (W)
p	pressure (Pa)
Q	flow rate ($m^3\ s^{-1}$)
R	resistance (Ω)
$\overline{R}$	ideal cell resistance (Ω)
r	resistance of manifold (Ω)
V	voltage (V)
V_0	open-circuit cell voltage (V)

Greek symbols

η	scaling-out efficiency
κ	electrolyte conductivity ($S\ m^{-1}$)
μ	fluid viscosity (Pa s)
σ	inconsistency coefficient
τ	flow resistance ($Pa\ s\ m^{-3}$)
χ	wetted perimeter (m)

Superscripts

max	maximum value

Subscripts

a	anolyte
c	catholyte
n	cell index
o	collection components
T	total amount

Abbreviations

OCV	open circuit voltage
RSD	relative standard deviation

List of tables

Table 1. Model parameters for the base case conditions.

List of figures

Fig. 1. (a) Assembly scheme of a M^2FC array consisting of four unit cells in a (a1) parallel connection and (a2) series connection. An enlarged view of a unit cell is given in (a3). (b) Photograph of the four-cell array. A Hong Kong dollar of 25.5 mm in diameter is place beside for size comparison. (c) Cross-sectional view SEM image of serpentine passages.

Fig. 2. Analog circuit of an *N*-cell array: (a) series array and (b) parallel array.

Fig. 3. (a) Comparison of flow distribution uniformity in the developed four-cell array and one with conventional straight-branch distributors. The flow rate data in the figure are the mean values from five independent measurements. The error bars represent standard deviations. The inset shows the effect of overall flow rate on flow distribution uniformity in the developed array. (b) An electronic-hydraulic analogy for the present array design: (b1) a schematic of the fluidic network in the present array. For simplicity, only two cells with half of the device geometry are considered; (b2) an equivalent electrical circuit. (c) Optical micrographs showing the interfacial species mixing in each unit cell channel at different flow rates under the present scaling-out strategy.

Fig. 4. Polarization and power curves of a single cell and four-cell array with different cell connections: (a) parallel connection and (b) series connection. Simulated curves from the shunt current model are also plotted in the same figures for comparison.

Fig. 5. (a) Model-predicted performance curves of the four-cell series array with serpentine-branch and straight-branch distributors by assuming $\sigma = 0$. (b) The scaling-out efficiency as a function of the ionic resistance of distribution branches. (c) Shunt current distributions in manifold and branch for different branch resistances. (d) Distributions of cell voltage and internal current for different branch resistances. (e) Shunt current distributions in manifold and branch for different manifold resistances. (f) Distributions of cell voltage and internal current for different manifold resistances.

Fig. 6. (a) Model-predicted performance curves of the four-cell series array for different degrees of cell behavior inconsistency. (b) The power efficiency as a function of the inconsistency coefficient at different discharge currents.

Fig. 7. (a) Shunt current distributions in manifold and branch for different numbers of cells in series. (b) Distributions of cell voltage and internal current for different numbers of cells in series. (c) The scaling-out efficiency as a function of the number of cells in series for different branch resistances. (d) Distributions of branch current and cell voltage for different branch resistances. (e) The scaling-out efficiency as a function of the number of cells for different cell resistances. (f) Distributions of branch current and cell voltage for different cell resistances. All of the simulations in the figure were conducted at $\sigma = 0$.

Table 1. Model parameters for the base case conditions.

Parameters	Value	Note
Channel length, L	28.14 cm for each serpentine branch; 2.72 cm for the straight branches connecting with cell 2 and cell 3; 3.46 cm for the straight branches connecting with cell 1 and cell 4; 0.2 cm for distribution manifolds.	Measured value
Cross-sectional area of channel, A	0.00049 cm^2 for serpentine channels; 0.005 cm^2 for straight channels; 0.025 cm^2 for distribution manifolds.	Measured value
Anolyte conductivity, κ_a	247 mS cm^{-1}	Measured value
Catholyte conductivity, κ_c	244 mS cm^{-1}	Measured value
Open-circuit cell voltage, V_0	0.747 V	Measured value

Fig. 1

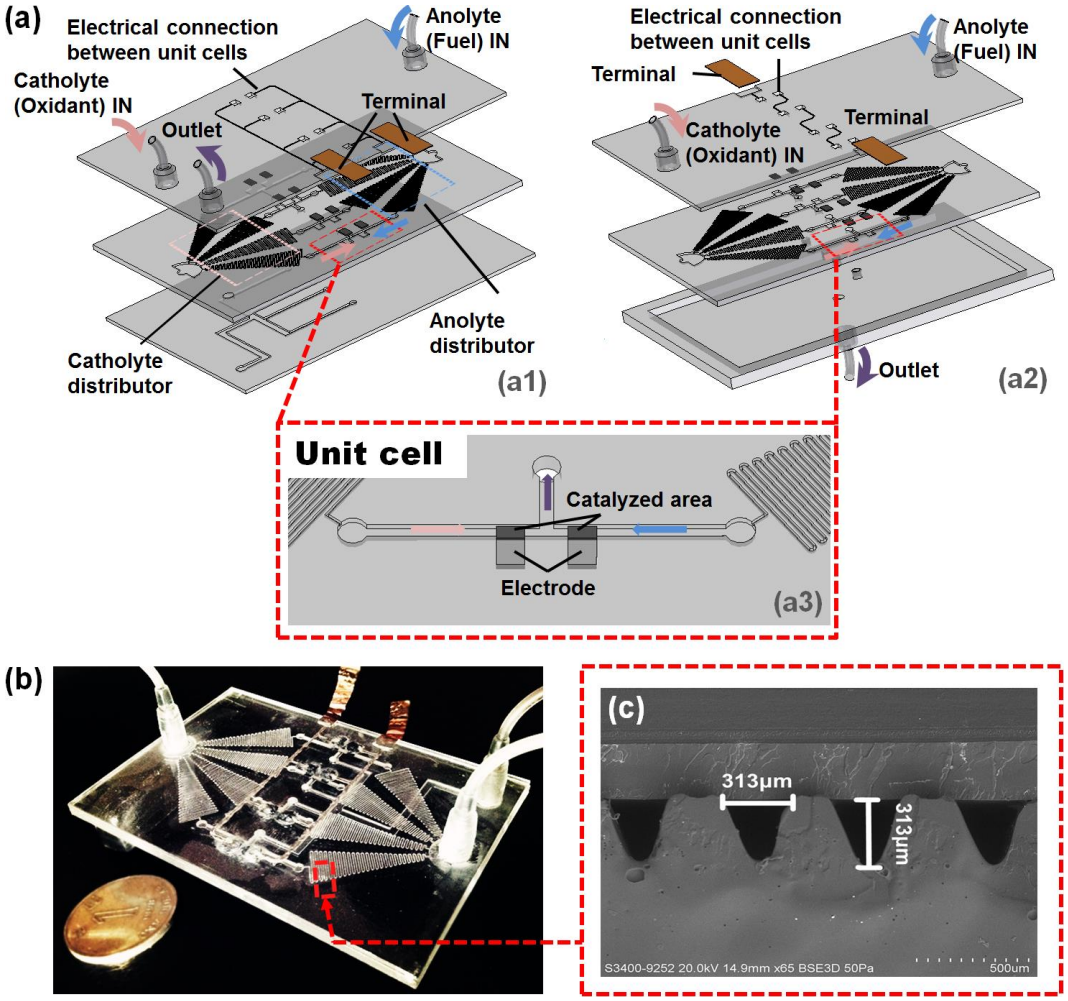
(a)
Electrical connection between unit cells
Anolyte (Fuel) IN
Catholyte (Oxidant) IN
Outlet
Terminal
Anolyte distributor
Catholyte distributor
(a1)
Electrical connection between unit cells
Terminal
Anolyte (Fuel) IN
Catholyte (Oxidant) IN
Terminal
Outlet
(a2)
Unit cell
Catalyzed area
Electrode
(a3)
(b)
(c)
313μm
313μm
S3400-9252 20.0kV 14.9mm x65 BSE3D 50Pa
500um

Fig. 2

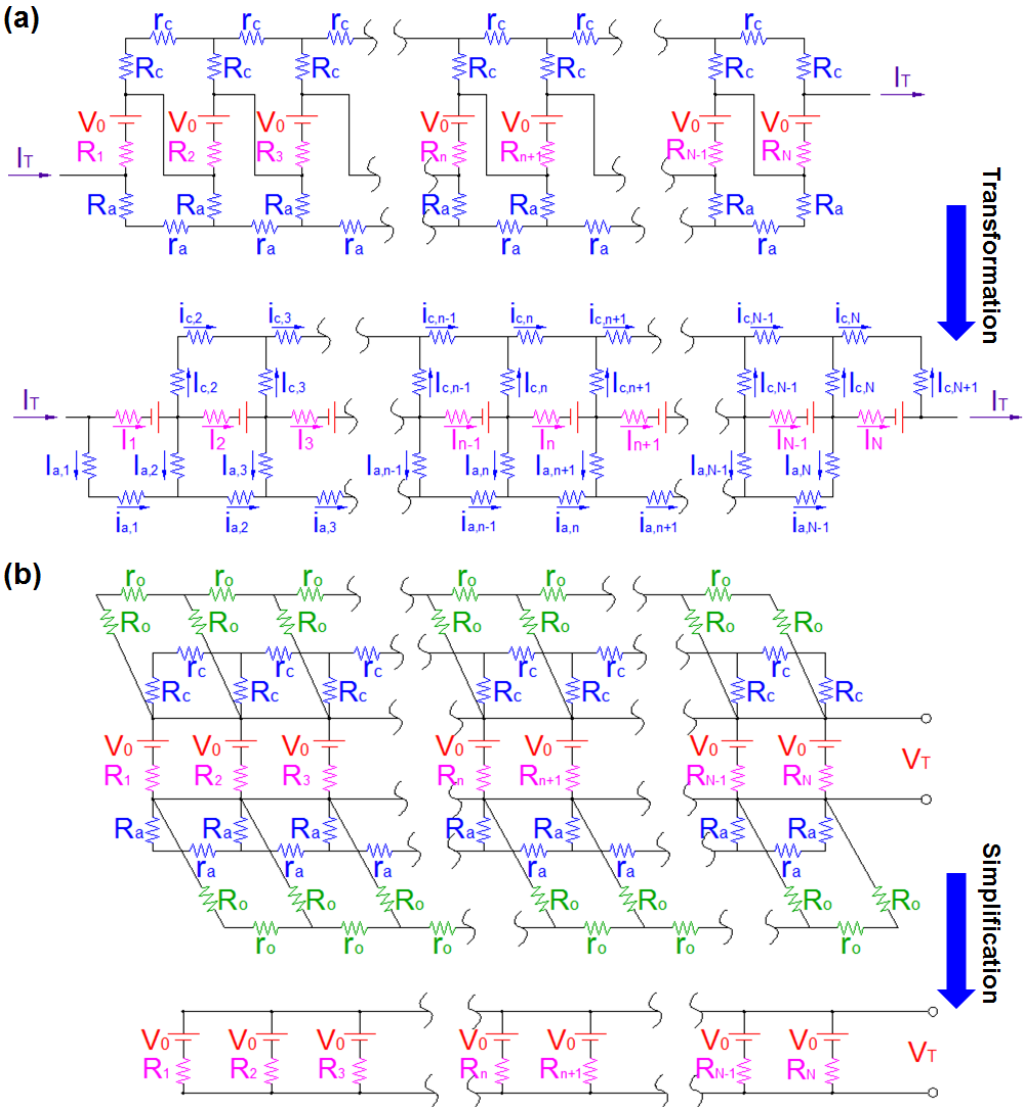

Fig. 3

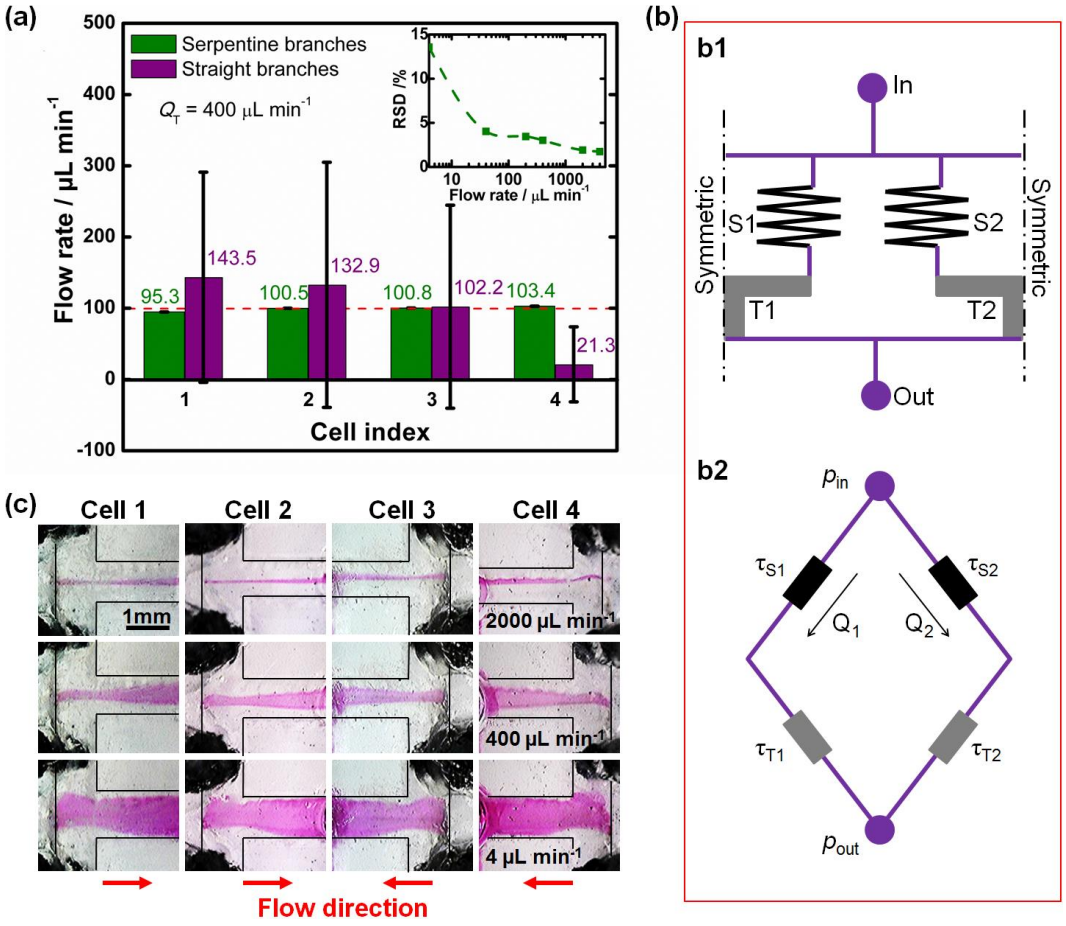
(a)
Serpentine branches
Straight branches
Q_T = 400 μL min^{-1}
Flow rate / μL min^{-1}
Cell index
RSD /%
Flow rate / μL min^{-1}
95.3
143.5
100.5
132.9
100.8
102.2
103.4
21.3
(b)
b1
In
Out
Symmetric
Symmetric
S1
S2
T1
T2
b2
p_{in}
p_{out}
τ_{S1}
τ_{S2}
τ_{T1}
τ_{T2}
Q_1
Q_2
(c)
Cell 1
Cell 2
Cell 3
Cell 4
1mm
2000 μL min^{-1}
400 μL min^{-1}
4 μL min^{-1}
Flow direction

Fig. 4

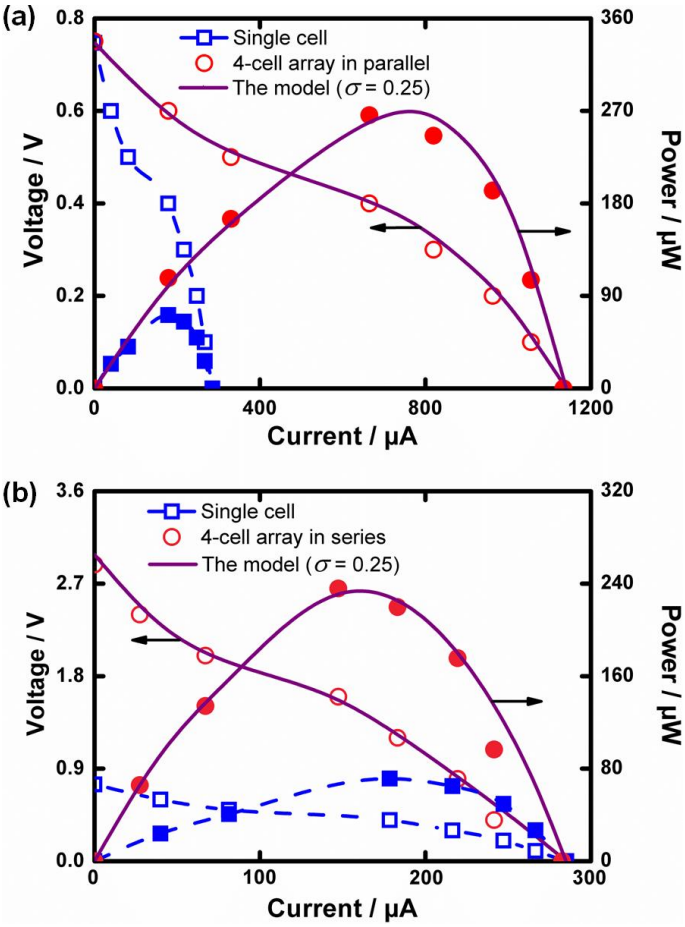
(a)
Single cell
4-cell array in parallel
The model (σ = 0.25)
Voltage / V
Power / μW
Current / μA
0.0
0.2
0.4
0.6
0.8
0
90
180
270
360
0
400
800
1200
(b)
Single cell
4-cell array in series
The model (σ = 0.25)
Voltage / V
Power / μW
Current / μA
0.0
0.9
1.8
2.7
3.6
0
80
160
240
320
0
100
200
300

Fig. 5

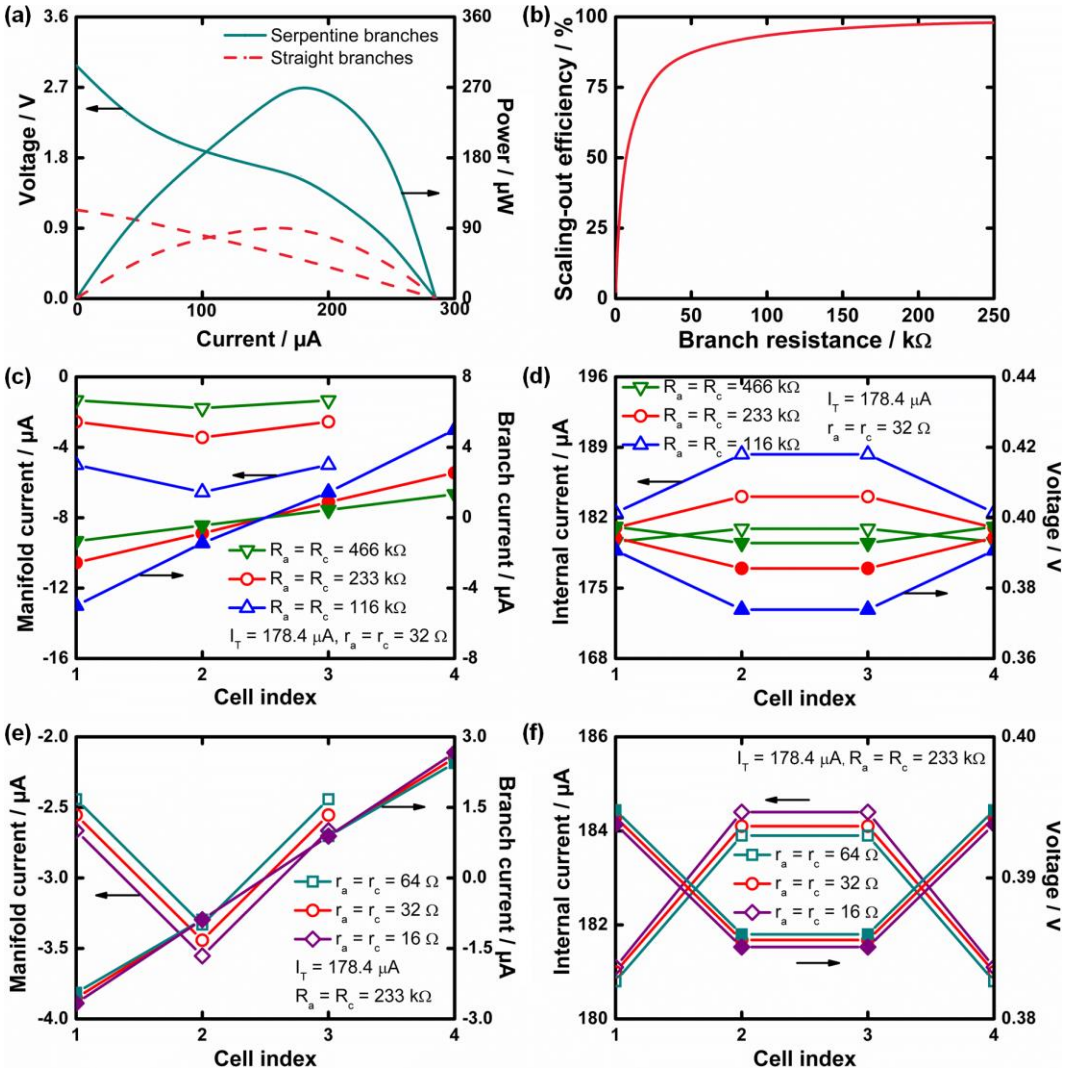
(a)
Serpentine branches
Straight branches
Voltage / V
Power / μW
Current / μA
(b)
Scaling-out efficiency / %
Branch resistance / kΩ
(c)
Manifold current / μA
Branch current / μA
Cell index
$R_a = R_c$ = 466 kΩ
$R_a = R_c$ = 233 kΩ
$R_a = R_c$ = 116 kΩ
I_T = 178.4 μA, $r_a = r_c$ = 32 Ω
(d)
Internal current / μA
Voltage / V
Cell index
I_T = 178.4 μA
$r_a = r_c$ = 32 Ω
(e)
Manifold current / μA
Branch current / μA
Cell index
$r_a = r_c$ = 64 Ω
$r_a = r_c$ = 32 Ω
$r_a = r_c$ = 16 Ω
I_T = 178.4 μA
$R_a = R_c$ = 233 kΩ
(f)
Internal current / μA
Voltage / V
Cell index
I_T = 178.4 μA, $R_a = R_c$ = 233 kΩ
$r_a = r_c$ = 64 Ω
$r_a = r_c$ = 32 Ω
$r_a = r_c$ = 16 Ω

Fig. 6

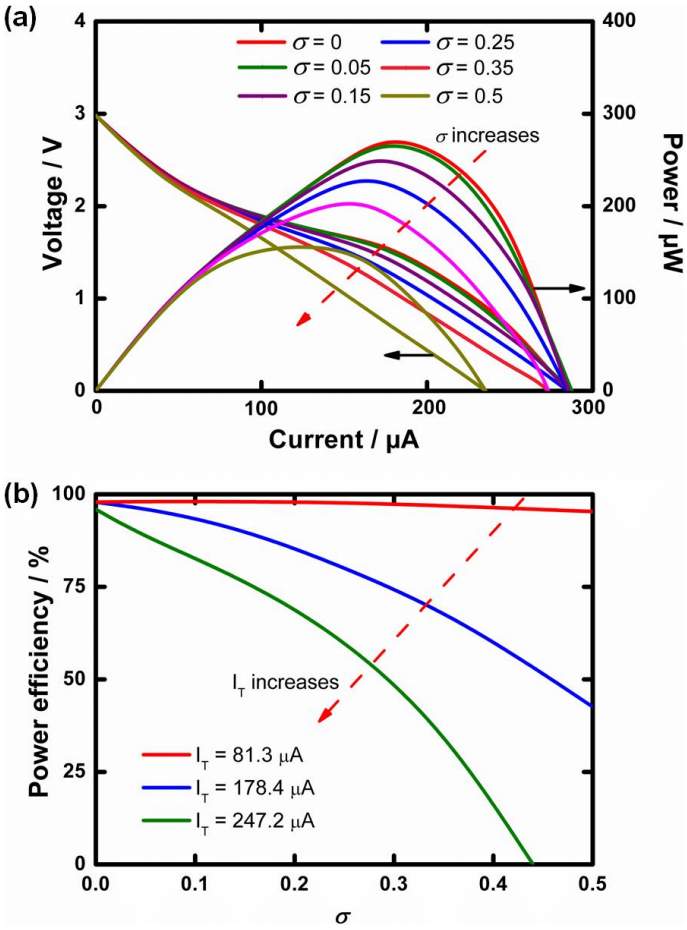
(a)
σ = 0
σ = 0.25
σ = 0.05
σ = 0.35
σ = 0.15
σ = 0.5
σ increases
Voltage / V
Power / μW
Current / μA
(b)
Power efficiency / %
I_T increases
I_T = 81.3 μA
I_T = 178.4 μA
I_T = 247.2 μA
σ

Fig. 7

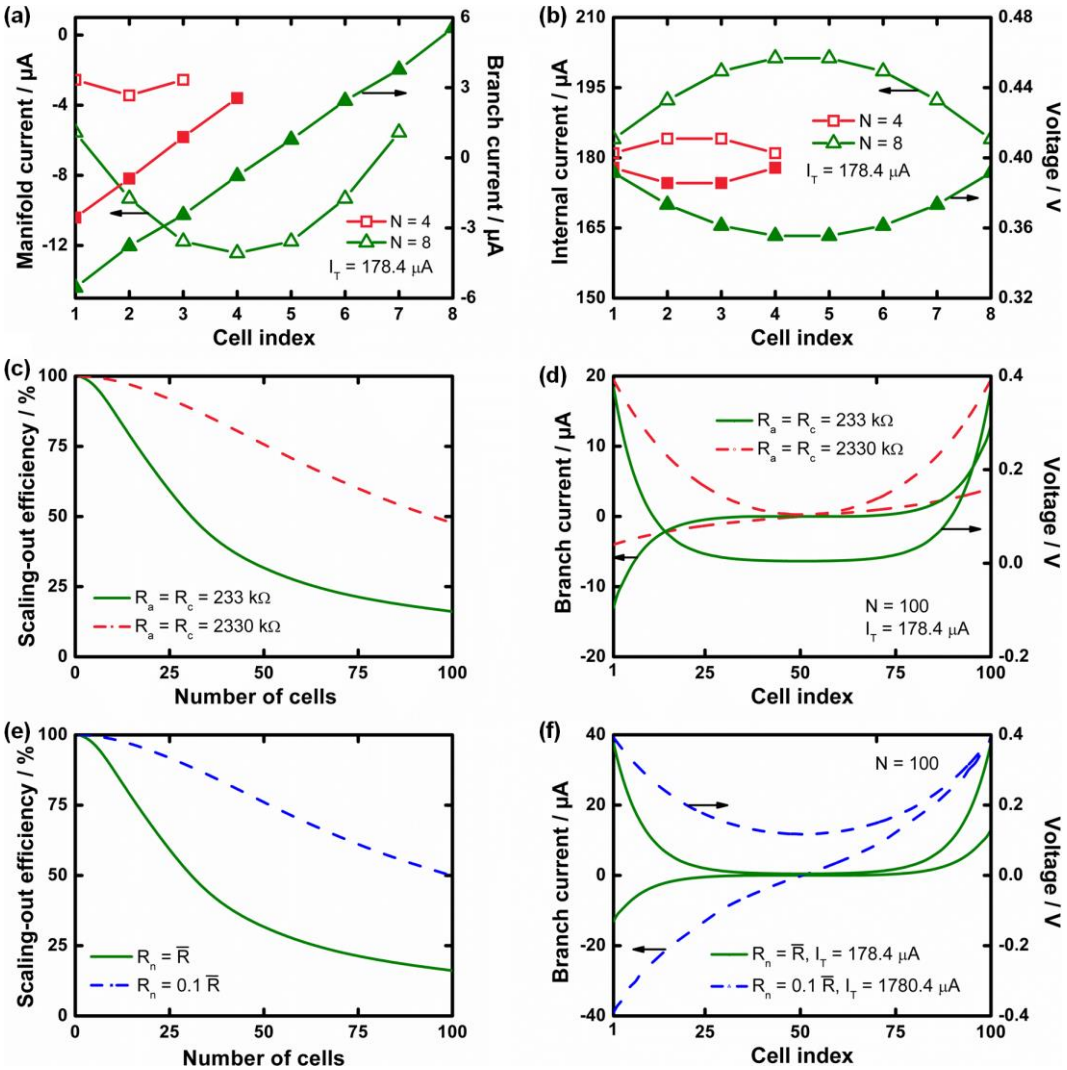
(a)
Manifold current / μA
Branch current / μA
Cell index
N = 4
N = 8
I_T = 178.4 μA
(b)
Internal current / μA
Voltage / V
Cell index
N = 4
N = 8
I_T = 178.4 μA
(c)
Scaling-out efficiency / %
Number of cells
R_a = R_c = 233 kΩ
R_a = R_c = 2330 kΩ
(d)
Branch current / μA
Voltage / V
Cell index
R_a = R_c = 233 kΩ
R_a = R_c = 2330 kΩ
N = 100
I_T = 178.4 μA
(e)
Scaling-out efficiency / %
Number of cells
R_n = R̄
R_n = 0.1 R̄
(f)
Branch current / μA
Voltage / V
Cell index
N = 100
R_n = R̄, I_T = 178.4 μA
R_n = 0.1 R̄, I_T = 1780.4 μA